

Coarse-Grained Molecular Dynamics Simulation of Ammonium Surfactant Self-Assemblies: Micelles and Vesicles

Rongliang Wu, Manli Deng,[†] Bin Kong, and Xiaozhen Yang*

Beijing National Laboratory for Molecular Sciences (BNLMS), Joint Laboratory of Polymer Science and Materials, Key Laboratory of Colloid and Interface Sciences, Institute of Chemistry, Chinese Academy of Sciences, Beijing 100190, P. R. China

Received: June 29, 2009; Revised Manuscript Received: September 26, 2009

Large-scale coarse-grained molecular dynamics simulations have been performed to investigate the self-assemblies of dodecyltrimethylammonium bromide (DTAB) and gemini surfactants 12-*S*-12 (*S* = 6, 14, and 20). At the concentrations investigated, the surfactants experience fast aggregation of monomers into oligomers until the cluster numbers reach maxima. For DTAB, larger aggregates grow at the expense of monomers, but for gemini surfactants, the growth of clusters is accomplished via the merging of oligomers. In the final stage, spherical and worm-like micelles coexist in the systems of DTAB and 12-6-12, and in gemini systems with longer spacers, namely, 12-14-12 and 12-20-12, well-defined vesicles are formed through expansion and curving of bilayer-like structures. Through detailed analysis of the vesicle structures, many of the 12-20-12 surfactants are found to have their headgroups at different surfaces, with the spacers bridging the inner and outer surface of the vesicle.

1. Introduction

Gemini surfactants, which consist of two conventional single-chain surfactants covalently attached by a spacer group, have been drawing increased attention owing to their unique properties of remarkably low critical micelle concentration (CMC) and unusual aggregation morphologies.¹ These specialties have led to various applications in detergency, the food industry, and petroleum recovery.² The most common series of gemini surfactants are the cationic alkanediyl- α,ω -bis(dodecyldimethylammonium bromide) surfactants with the structures of $[\text{C}_{12}\text{H}_{25}(\text{CH}_3)_2\text{N}(\text{CH}_2)_S\text{N}(\text{CH}_3)_2\text{C}_{12}\text{H}_{25}]\text{Br}_2$, which are referred to as 12-*S*-12, Br₂. In previous decades, extensive experimental and theoretical investigations have been performed on their adsorption behavior at surfaces, self-assembly, rheology, phase behavior, as well as interactions with macromolecules.^{1–4} However, atomistic molecular insight into such complex systems is still not easily obtained from both theory and experiments.

With the fast development of computational technologies, molecular simulations have proven more and more valuable for the study of complex systems. Recently, atomistic molecular dynamics (MD) simulations have been extensively used to investigate the behavior of surfactants at air/water^{5–8} or oil/water^{9–11} interfaces. In these simulations, due to the limited size (within ~ 10 nm) of the affordable systems, the investigation of surfactant self-assembly in the bulk phase is not possible. In the mean time, there are also cases^{12–15} where the aggregation behaviors of 40–125 single-tail surfactants in solutions are simulated with the absence of interfaces using atomistic MD. Though the micelle formation, fragmentation, and monomer exchange with the surroundings could be observed, the simulation times were limited to at most tens of nanoseconds. The aggregation of long surfactants, such as the gemini surfactants, is hard to obtain according to our experience. All-atom (AA) MD simulations have been performed to investigate the mo-

lecular organization of gemini surfactants in cylindrical micelles.¹⁶ While the structures of the cylindrical micelles are predefined instead of self-assembled, up to now quantitative atomistic simulations of gemini surfactant self-assemblies are not seen.

Coarse-grained molecular dynamics (CGMD)^{17–20} considerably enhances our ability to access the self-assembly process.²¹ Pioneering work by Smit²⁰ applied CGMD to lipid systems, and now a large variety of coarse graining approaches are available, ranging from the qualitative models and solvent-free models to models including more chemical specificity.²² The qualitative simulations of gemini surfactant self-assemblies date back to 1994, when Karaborni et al.²³ reported their results of the self-assemblies of gemini surfactants with different spacer lengths. In their simulations, spherical and thread-like micelles were obtained, respectively, for single-chain and gemini surfactants, and it was found that with longer spacers tree-like micelles were spontaneously formed. Later, Maiti et al.²⁴ utilized the lattice models to investigate the gemini surfactant self-assemblies in water and at air–water interfaces, in which properties of CMC and headgroup coverage areas against spacer or tail length were obtained. Only recently, Marrink et al.²² have systematically parametrized an extended version of semiquantitative coarse-grained interaction potentials, called the MARTINI force field, to describe biomolecular systems. The force field includes four main types of interaction sites and 18 subtypes, and its CGMD simulation results compared well with those atomistic simulations in the stress profiles across a lipid bilayer and the potential of mean force for extracting or traversing a lipid through a bilayer.¹⁸ The MARTINI force field also leads to good agreement with experiments for properties such as the density, diffusion, surface area per headgroup, interfacial tension, spontaneous curvature, and conditions for a lamellar to micelle transition.^{22,25,26}

In the present work, the potential parameters of the MARTINI force field have been utilized to investigate the self-assemblies of cationic ammonium surfactants through large-scale CGMD

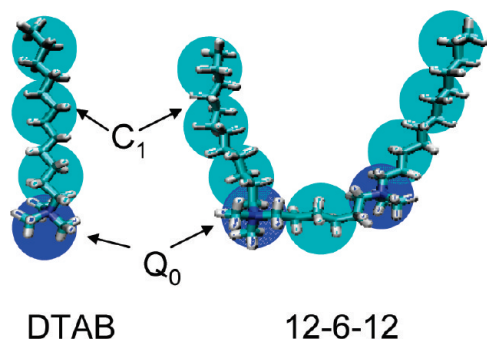
* To whom correspondence should be addressed. E-mail: yangx@iccas.ac.cn.

[†] Key Laboratory of Colloid and Interface Sciences.

TABLE 1: Information of Simulated Systems

systems	$N_{\text{water}} (\times 10^{-3})^a$	N_{sur}	L (nm)	C (mM)
DTAB (AA)	12.604	90	6.35	584.2
DTAB (CG)	983.484	2000	31.25	108.9
12-6-12 (CG)	980.672	1000	31.25	54.42
12-14-12 (CG)	976.016	1000	31.29	54.22
12-20-12 (CG)	970.632	1000	31.31	54.14

^a The water numbers are 4 times that of the water beads in our systems since the Martini force field uses 4-1 mapping for water molecules.

**Figure 1.** Mapping between AA structure and CG beads for DTAB and 12-6-12.

simulations, in which the systems are orders of magnitude larger than those in atomistic simulations. Micelle structure of the single-tail surfactant, *n*-dodecyltrimethylammonium bromide (DTAB), is also compared with our AAMD simulations.

2. Methods

Large-scale CGMD simulations have been carried out for the bulk solutions of cationic ammonium surfactants, DTAB, 12-6-12, 12-14-12, and 12-20-12, in which the DTAB system is also investigated by AA models. In fact, we have also tried to model the self-assemblies of gemini surfactants by AA models, but none of them gave well-defined micelles or vesicles. All CG systems contain 2000 headgroups in cubic boxes of ~ 30 nm, thus the concentrations are ~ 50 mM for gemini surfactants and ~ 100 mM for DTAB. The detailed information of molecule numbers, equilibrium system sizes L , and concentrations C is listed in Table 1.

The Martini force field²² includes four main types of interaction sites: polar (P), nonpolar (N), apolar (C), and charged (Q), and each has a number of subtypes (represented by subscripts) allowing for more accurate representations of chemical structures. For our systems, only four sorts of interaction sites are necessary: C_1 for hydrocarbon groups, Q_0 for ammonium headgroups (N and three of its connected carbon atoms), Q_a for the bromide ion, and P_4 for water. The common 4-1 mapping scheme for DTAB and 12-6-12 is sketched in Figure 1. The DTAB is represented by three C_1 beads and a Q_0 bead; 12-6-12 is represented by two such chains connected by a C_1 bead as the spacer; 12-14-12 has three C_1 beads as the spacer. The spacer of 12-20-12 is represented by 5 C_1 beads, whose masses are mapped by 3.6-1 instead of 4-1 according to the mapping scheme of alkanes with various lengths.¹⁸ In our simulations, all beads are assigned realistic masses so that accurate kinetic properties can be obtained.²² The standard conversion factor of 4 is still used for time scale interpretation unless otherwise noted.

The form of CG interaction potentials remains similar with those of atomistic simulations (eq 1) in the Martini force field.²²

$$V = \frac{1}{2}k_b(l - l_0)^2 + \frac{1}{2}k_\theta[\cos(\theta) - \cos(\theta_0)]^2 + 4\epsilon\left[\left(\frac{\sigma}{r_{ij}}\right)^{12} - \left(\frac{\sigma}{r_{ij}}\right)^6\right] + \frac{q_i q_j}{4\pi\epsilon_0\epsilon_r r_{ij}} \quad (1)$$

The bonds are described by the weak harmonic potential with equilibrium bond lengths $l_0 = 0.47$ nm and force constant $k_b = 1250$ kJ mol⁻¹ nm⁻² for all bonds involved in our systems. The cosine type weak harmonic potential is used for all angles with force constants $k_\theta = 25$ kJ mol⁻¹, and the equilibrium bond angle $\theta_0 = 180^\circ$ except for the angle formed among tail, head, and spacer (C_1 - Q_0 - C_1) beads whose $\theta_0 = 90^\circ$. The nonbonded interactions are also described by the Lennard-Jones (L-J) 12-6 potential energy function and the shifted Coulombic potential energy function for charged beads ($Q_0 = +1$ and $Q_a = -1$) with relative dielectric constant $\epsilon_r = 15$ for explicit screening.²² The nonbonded interactions are excluded only between bonded beads, while those between second nearest neighbors are not.²² The L-J parameters for beads and interaction pairs involved in our systems are listed in Table 2 for convenience.

The CGMD simulations were carried out using the GRO-MACS 4.0²⁷ MD simulation package, and equations of motion were integrated with the leapfrog algorithm with a time step of 0.03 ps. NPT (constant pressure and constant temperature) ensembles with periodic boundary conditions for the cubic simulation boxes were used. The temperatures were coupled to 300 K by the velocity rescaling method,²⁸ and the pressures were coupled to 1 bar by the Berendsen method.²⁹ The cutoff for nonbonded interactions is set to be 1.2 nm with the standard shift functions of GROMACS, where the L-J potential is shifted from 0.9 to 1.2 nm and the electrostatic potential is shifted from 0 to 1.2 nm, which mimics the effect of a distance-dependent screening.²²

Our AAMD simulations refer to that of Jorge,¹⁵ who successfully performed the MD simulation of the self-assembly of decyltrimethylammonium bromide (DeTAB) with atomistic models. Our system contains 90 DTAB molecular pairs in a ~ 6 nm cubic box. The TIP4P rigid water model³⁰ and the OPLS all-atom force field³¹⁻³³ were used. The rigid structure of water was maintained using the Settle method,³⁴ and the bond lengths of all other molecules were constrained with the LINCS algorithm.³⁵ The initial conditions were set to be a bilayer-like structure to accelerate the self-assembly process, and an 8 ns run was performed to obtain two well-defined micelles. The time step used was 1 fs, and the trajectories were recorded every 1 ps. The temperature was controlled by the Nose-Hoover thermostat at 300 K, and the pressure was controlled by the Parrinello-Rahman barostat at 1 bar. A twin-range cutoff of 1.0-1.2 nm was employed, and the long-range dispersion corrections were also implemented for both energy and pressure.

TABLE 2: Non-bonded interaction parameters

atom type or pairs	ϵ (kJ/mol)	σ (nm)
C_1	3.5	0.47
Q_0	3.5	0.47
Q_a	5.0	0.47
P_4	5.0	0.47
C_1, Q_0	2.0	0.62
C_1, Q_a	2.0	0.62
C_1, P_4	2.0	0.47
Q_0, Q_a	4.5	0.47
Q_0, P_4	5.6	0.47
Q_a, P_4	5.6	0.47

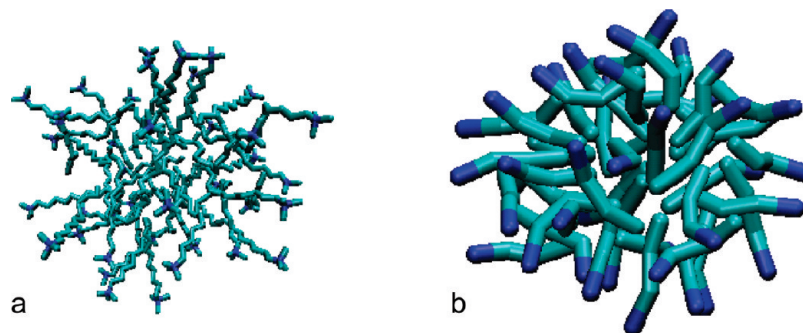


Figure 2. Snapshots of micelles for (a) AA model with $N = 40$ and (b) CG model with $N = 42$. Hydrogen atoms are not shown in the AA model for clarity.

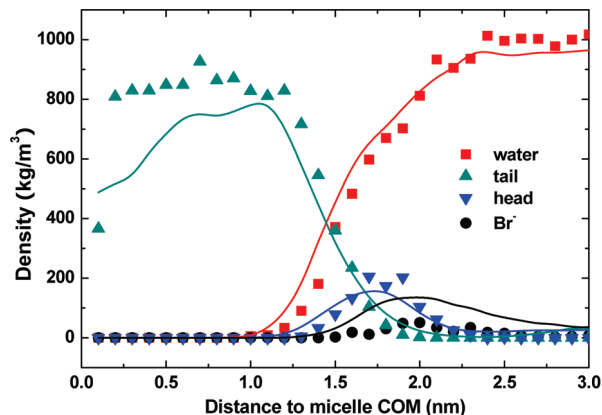


Figure 3. Density profiles of micelles with respect to COMs for AA (line) and CG (symbols) models.

The long-range electrostatics were handled using the Particle Mesh Ewald (PME) method.^{36,37}

3. Results and Discussions

3.1. AA and CG Micelle Structures. In MD simulations, we can trace the behavior of all clusters formed. The properties of clusters are analyzed with the *g_clustsize* program in GROMACS,²⁷ slightly modified to output more information such as cluster size, cluster structure, as well as monomer concentration. In the program, two molecules are regarded as belonging to the same cluster when any of their tail particles are separated by no more than a cutoff distance. The cutoffs are set to 0.5 nm which is smaller than the first minima of the radial distribution functions between tail particles, and the output results of cluster numbers and aggregations are well checked with visual inspections.

The snapshots of AA and CG micelles with aggregation numbers of 40 and 42, respectively, are given in Figure 2, whose density profiles with respect to their own centers of mass (COM) are plotted in Figure 3. The densities are averages near the end of the trajectories, when the two micelles are in relatively stable configurations. The densities of both models correspond very well with each other.

The dividing plane between hydrophilic and hydrophobic domains is at ~ 1.4 nm, which can be taken to calculate the area per surfactant molecule. The position of the dividing plane is not taken at the peak of headgroup density because the headgroups are immersed in the hydrophilic phase and do not well signify the interface between the hydrophobic and hydrophilic parts. To be consistent with the experimental conditions and regular planes in simulations,³⁸ the intersection between densities of water and the hydrophobic part is used instead of

the maximum in headgroup density. For the aggregation number $N_{ag} = \sim 40$, the surface area per headgroup $A_{head} = \sim 0.615$ nm², which is in good agreement with the experimental value³⁹ at the water/vapor surface (0.45 nm²). The CG ions are more dispersive and have a lower concentration around the headgroups than that of AA ones, while they still have a similar peak position with the AA model around 0.3 nm away from the headgroup, which are similar with that reported for DeTAB.¹⁵ From the distributions, we can also see that water can diffuse more than 0.5 nm into the micelle.

3.2. Micelle Formation Processes for DTAB and 12-6-12.

The micelle formation processes of DTAB and 12-6-12 are shown by snapshots in Figure 4. Both systems evolve from random initial states to small aggregates at ~ 10 ns (not shown for 12-6-12), then into spherical micelles at ~ 100 ns, and finally some of the micelles merge into long worm-like micelles. For DTAB, the spherical micelles still take the majority at the final stages of our simulation, while for 12-6-12, the long worm-like micelles can be clearly seen at the final stage.

The cluster size distributions, including the monomers, at different time stages are displayed in Figure 5. The oligomers at the initial stages are composed of 5–10 surfactants for both DTAB and 12-6-12. At later stages, the collisions among these oligomers lead to the formation of larger aggregates, and the size distributions move to the larger N_{ag} side. In the final stage, the cluster size distributions can be divided into the monomer or oligomer region and the micelle region. For 12-6-12, split micelle distributions are obtained due to the still too small number of surfactants for good statistics with the large N_{ag} value of 12-6-12. It is clear that only aggregates with $N_{ag} > 10$ can be regarded as well-defined micelles,⁴⁰ and the following results will use this cutoff to distinguish between micelles and oligomers.

More quantitative information on the micelle formation processes can be illustrated by the evolutions of monomer number, cluster number, and average cluster size with simulation time in Figure 6. Both cluster numbers reach maxima within tens of nanoseconds.

For DTAB, the monomer number reaches basic equilibrium when the cluster size reaches the first plateau, which means the cluster size still grows at the expense of monomers after the formation of oligomers. Further increments of cluster size are not accompanied by distinct decreases of monomers, demonstrating that these processes are accomplished via merging between small micelles. In the final stage of DTAB, over 30 micelles of average size ~ 50 are formed, which is in reasonable agreement with the experimental aggregation numbers of 55–57.^{41,42}

For 12-6-12, the monomer number shows no decrease when the cluster number reaches maximum, thus only the oligomer

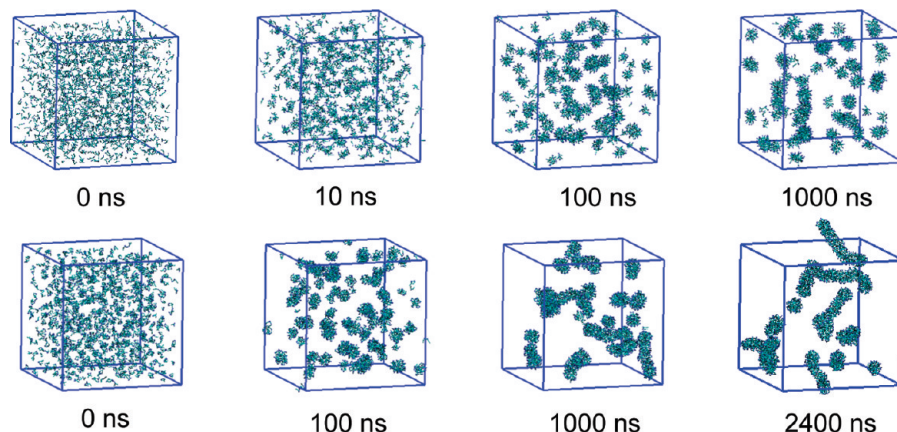


Figure 4. Snapshots of micelle formation processes at different time stages for DTAB (upper panel) and 12-6-12 (lower panel).

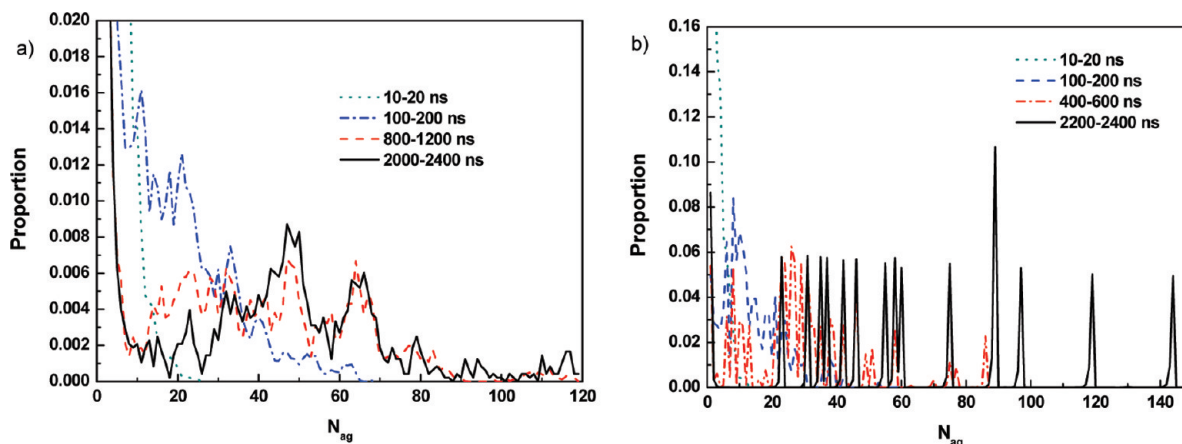


Figure 5. Size distributions of clusters at different time stages for (a) DTAB and (b) 12-6-12.

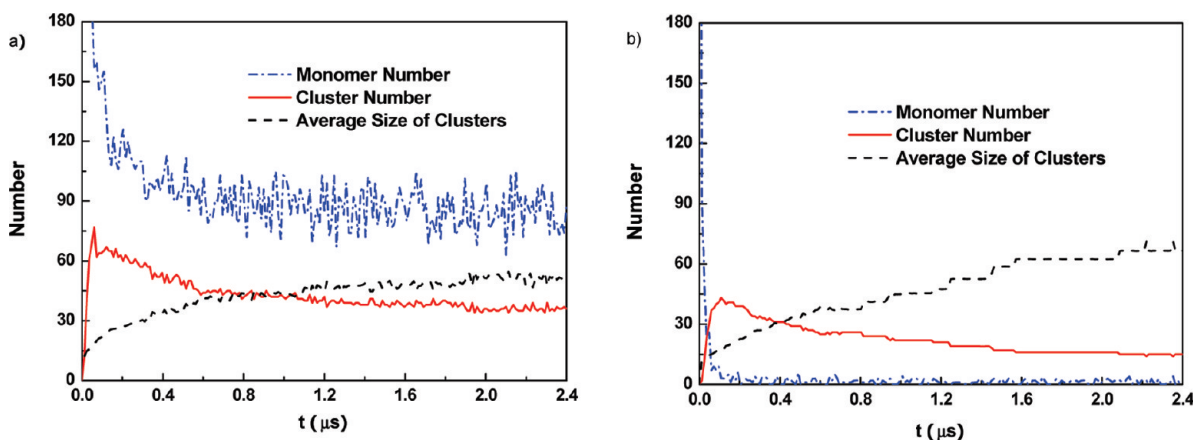


Figure 6. Evolutions of monomer numbers, cluster numbers, and average sizes of clusters ($N_{ag} > 10$) for (a) DTAB and (b) 12-6-12.

formation is associated with the monomers and the further increase of cluster size is mainly due to the merging of small aggregates for 12-6-12. At later stages from microseconds on, the micelles continue to form even longer worm-like micelles. Due to the merging and disruption of long micelles, the cluster number and size still have occasional jumps after 2.2 μs . The average cluster size of 67 at the final stage is larger than the experimental value of 52 at 10 mM⁴³ since a higher concentration usually leads to larger aggregation numbers.

In general, the micelle formation processes can be divided into three stages: the fast aggregation of monomers into small disordered oligomers until the number of clusters reaches a maximum in around tens of nanoseconds; the ripening process

by which larger aggregates grow at the expense of smaller ones or monomer and the total number of clusters decreases with time evolution; within microseconds, the micelle number reaches a relatively stable value, though micelle merging and disruption still exist.

3.3. Micelle Radius of Gyration. For spherical micelles, the sizes can be easily determined from density profiles as illustrated in Figure 3, while 12-6-12 can form longer worm-like micelles than that of DTAB at the same overall headgroup concentration. The representative snapshots of large single worm-like micelles of DTAB and 12-6-12 are given in Figure 7. The number of chains or headgroups for 12-6-12 is nearly 3 times that of DTAB.

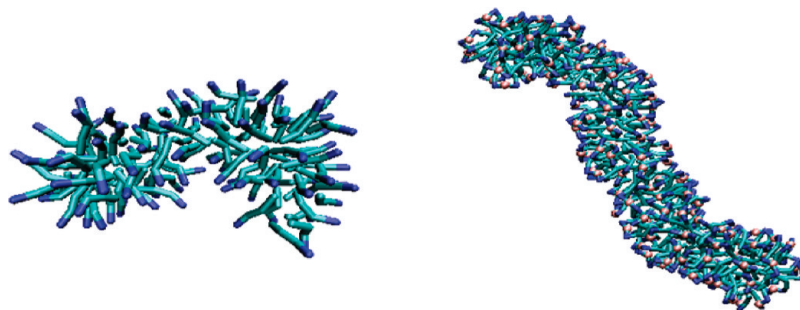


Figure 7. Snapshots of the long worm-like micelles of DTAB (left) and 12-6-12 (right) with aggregation numbers of 107 and 144, respectively. The pink colored beads represent the spacers of 12-6-12.

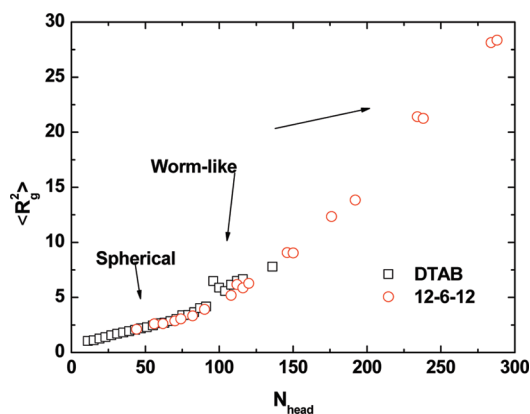


Figure 8. Mean square radius of gyration against aggregation numbers of headgroups. The distinction between spherical and worm-like micelle is around $N_{\text{head}} = 90$.

For both shapes, the more quantitative information on micelle size can be obtained through the mass weighed mean square radius of gyration

$$\langle R_g^2 \rangle = \frac{\sum_i^{N_{\text{ag}}} m_i (\mathbf{r}_i - \mathbf{r}_{\text{cm}})^2}{\sum_i^{N_{\text{ag}}} m_i} \quad (2)$$

where m_i is the mass of bead i in a micelle with aggregation number of N_{ag} ; \mathbf{r}_i is the position vector of bead i ; and \mathbf{r}_{cm} is the position vector of the micelle center of mass; thus $(\mathbf{r}_i - \mathbf{r}_{\text{cm}})^2$ represents the squared distance from bead i to the micelle center of mass and the angle bracket represents ensemble average among micelles with the same aggregation numbers. The square radii of gyration for DTAB and 12-6-12 are plotted against the micelle headgroup number in Figure 8. At lower N_{head} ($< \sim 90$) micelles are spherical, whose mean square radii of gyration for both DTAB and 12-6-12 have a very good linear relationship with N_{head} . For spheres, $R_g^2 = 3R^2/5$,⁴⁴ where R is the sphere radius. Thus, the ensemble average area per headgroup A_{head} can be estimated by the slope $4\pi R^2/N_{\text{head}} = 20\pi R_g^2/3N_{\text{head}} = 0.714 \text{ nm}^2/\text{head}$ for spherical micelles. For the worm-like micelles, R_g^2 and N_{head} have more complicated relations, while it can be seen that the worm-like micelles for DTAB and 12-6-12 are still similar in nature with $N_{\text{head}} = \sim 120$, albeit the existence of the connecting spacers in 12-6-12.

3.4. Vesicle Formation and Structure. With longer spacers, gemini surfactants can often self-assemble into bilayers or vesicles. The snapshots of the 12-20-12 self-assembly process

are shown in Figure 9, and the formation of 12-20-12 vesicles is more complicated: first, small spherical micelles are formed at around 100 ns, then the micelles integrate into small planar bilayer-like structures at ~ 500 ns. The bilayers expand and curve into large spherical vesicles within microseconds. Finally, the system forms two spherical vesicles and an open vesicle, which is also seen by TEM of a 1.4% 12-20-12 solution in experiments,⁴⁵ though our vesicles obtained are much smaller than those seen in experiments.

For 12-14-12, the process is much the same way as that of 12-20-12, but the vesicles formed are smaller (not shown) as seen from the time evolutions of average cluster size in Figure 10. It seems that the evolution of cluster and monomer numbers for geminis is very similar, whether they form micelles or vesicles. Namely, only the oligomer formation is associated with the decrease of monomer number until the cluster number reaches maxima, and the further increase of cluster size is mainly due to the merging of small aggregates; however, for a single-tail surfactant like DTAB, the aggregates grow at the expense of monomers. At later stages, smaller vesicles can still merge into larger ones as seen from both the snapshots and Figure 10, where boosts of average size take place.

The atomistic structure of the largest vesicle is shown in Figure 11, which is partly truncated for view of the inner structure. The headgroups, tails, and spacers are randomly distributed. Some surfactants have both heads at the same surface, while some others have one at the outer surface and the other at the inner surface, with their spacers bridging the two surfaces. Through detailed investigation of the inner structures, it is found that majorities of surfactants have only one headgroup at the inner surface.

The density profiles of each component with respect to its center of mass are given in Figure 12. The headgroup and counterion distributions split into two parts, signifying the two surfaces of the vesicle. It is clear that the headgroups and counterions at the inner surface are more compact than those at the outer surface, which supports the above observation that the inner surfaces are mostly populated with single headgroups. The spacer distribution does not divide into two separate peaks but just a single plateau of around $300 \text{ kg}/\text{cm}^3$, which shows that many of the surfactants have their spacers bridging the inner and outer surface. With some of the spacers bent toward the interior of the vesicle at the outer surface, the density of the spacer close to the outer surface is slightly larger.

The inner and outer surfaces of the 12-20-12 vesicle have 399 and 575 headgroups, respectively, and the dividing planes between hydrophilic and hydrophobic domains are found to be around 4.2 and 6.1 nm, which are the intersections between the density curves of water and the total hydrophobic part. Thus, the surface areas per headgroup are 0.566 and 0.813 nm^2 ,

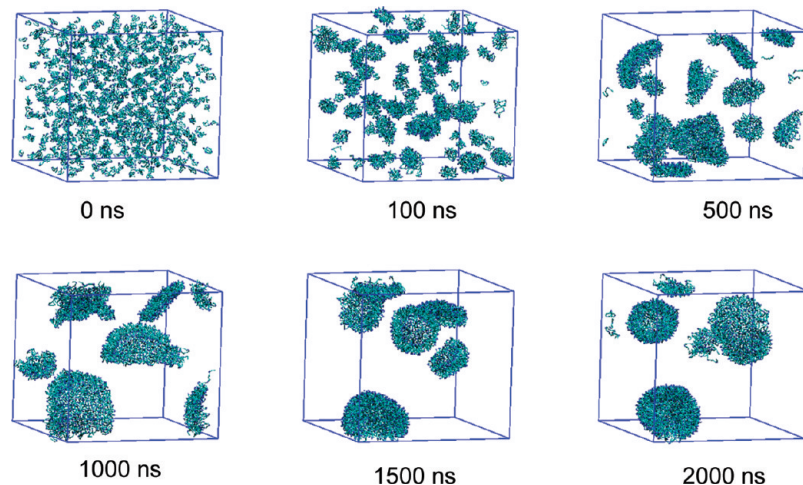


Figure 9. Snapshots of 12-20-12 self-assembly process at different time stages.

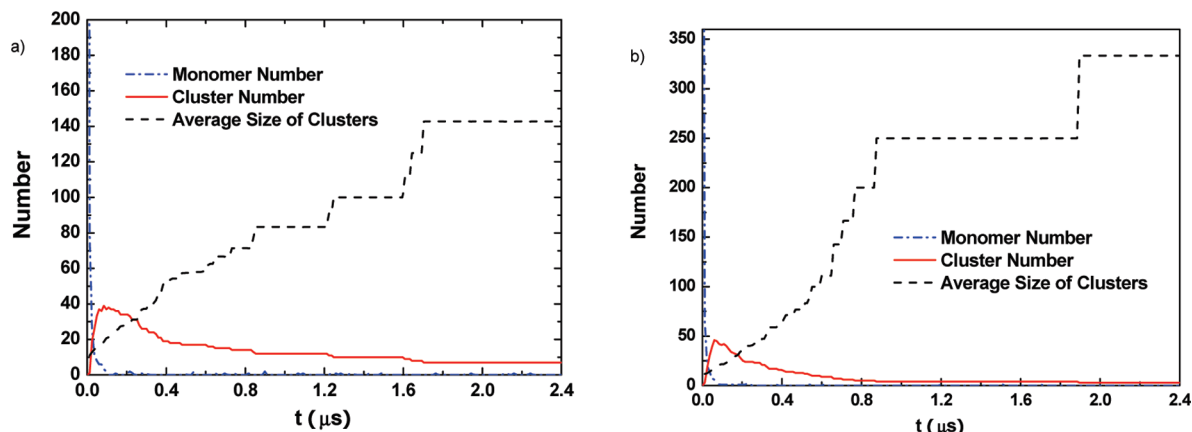


Figure 10. Evolutions of monomer numbers, cluster numbers, and average sizes of clusters ($N_{ag} > 10$) for (a) 12-14-12 and (b) 12-20-12.

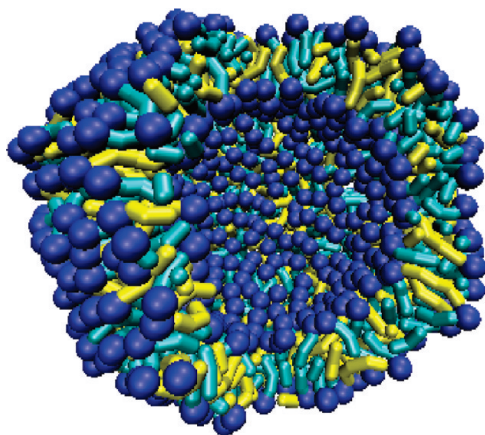


Figure 11. Partially truncated view of the largest vesicle formed with an aggregation number of 487. The blue beads are headgroups; the cyan bonds are tails; and the yellow bonds represent spacers.

respectively. In the same way, the average surface areas per headgroup for 12-14-12 are 0.754 and 1.105 nm², respectively, for the inner and outer surfaces of the vesicles formed. It is clear that the inner and outer surfaces of vesicles differ a lot in compactness. The outer surfactants occupy larger surfaces due to the existence of spacers on the interface, while those in the inner surface have almost all the spacers at the hydrophobic core, thus leading to a much smaller area per headgroup.

3.5. Property Changes with Spacer Length. Table 3 lists the area per headgroup and the equilibrium monomer concentrations (including oligomers with $N_{ag} < 10$) for all systems. These

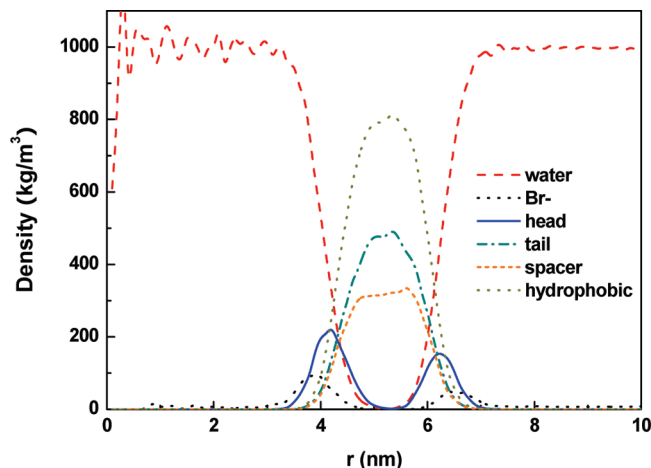


Figure 12. Density profiles of the 12-20-12 vesicle shown in Figure 11 with respect to its COM. The densities are averages of the last 400 ns.

values are compared with the interface area per headgroup obtained from surface tension measurements and experimental CMC.⁴⁵ For 12-6-12, the area per headgroup value is obtained from the R_g analysis in Section 3.3, while those of DTAB, 12-14-12, and 12-20-12 are obtained through the density profiles. Though the area per headgroup is different in nature from those adsorbed at the air/water interface, their values are very close to each other, and their variations with spacer length are in qualitative agreement.

TABLE 3: Surface Area Per Headgroup and Monomer Concentration

systems	A (nm ²)	A _{exp} (nm ²) ^a	C _{mon} (mM)	CMC (mM) ^a
DTAB	0.615	0.45	8.365 ± 1.181	15
12-6-12	0.714	0.715	0.086 ± 0.074	1.12
12-14-12	0.754 (inner) 1.105 (outer)	1.00	0.009 ± 0.021	0.18
12-20-12	0.566 (inner) 0.813 (outer)	<0.77	0	<0.1

^a Experimental values from the literature.⁴⁵

In principle, the monomer concentration in surfactant solutions close to CMC from above can be used as a rough estimate of CMC,² while both experiments² and recent simulations⁴⁶ showed that a larger surfactant concentration above CMC often leads to a smaller monomer concentration. Our systems have concentrations much larger than their CMC, and the monomer concentrations in Table 3 are smaller than the experimental CMC in all systems. To obtain monomer concentrations closer to the experimental CMC, larger systems with more water beads are necessary. With an increase of spacer length, the monomer concentration decreases, and for 12-20-12, even no monomers are observed. The variation of the monomer concentrations is consistent with that of the experimental CMC. All these show that the MARTINI coarse-grained model used in our simulations for the ammonium surfactants has enough accuracy to quantitatively investigate their self-assembly processes at the molecular level.

4. Conclusions

Large-scale CGMD simulations have been performed to investigate the self-assemblies of cationic ammonium surfactants. The structure of the DTAB micelle agrees perfectly with that obtained from AAMD simulations. In addition, the surface areas per headgroup and monomer concentrations of gemini surfactants are in good agreement with experiments.

The micelle formation processes of DTAB and 12-6-12 can be divided into three stages: the fast aggregation of monomers into small disordered oligomers until the number of clusters reaches a maximum; larger aggregates grow at the expense of smaller ones or monomer; the micelle number and size reaches a relatively stable value. At the investigated concentrations far above the experimental CMC, DTAB and 12-6-12 can both self-assemble into spherical and worm-like micelles, and the worm-like micelles of 12-6-12 can be much longer than those of DTAB.

The vesicle formation processes of 12-14-12 and 12-20-12 are a little more complicated, during which small planar bilayer-like structures through aggregation of small spherical micelles and the bilayers expand and curve into large spherical vesicles. 12-20-12 can form much larger vesicles than 12-14-12, and many of the spacers are found to bridge the two surfaces.

What is common for gemini surfactants during the self-assembly process is that only the oligomer formation is associated with the decrease of monomer number, and the further increase of cluster size is mainly due to the merging of small aggregates; however, for the single tail surfactant DTAB, the aggregates grow at the expense of monomers.

Later work will focus on the concentration dependence of the self-assembly kinetics of gemini surfactants.

Acknowledgment. This work was supported by the National Nature Science Foundation (20474073, 20490220, 20674090, and 90612015).

References and Notes

- (1) Menger, F. M.; Keiper, J. S. *Angew. Chem., Int. Ed.* **2000**, *39*, 1906.
- (2) Zana, R.; Xia, J. *Gemini surfactants: synthesis, interfacial and solution-phase behavior, and applications*; Marcel Dekker: New York, 2004.
- (3) Wang, X.; Wang, J.; Wang, Y. Y.; H.; Li, P.; Thomas, R. K. *Langmuir* **2004**, *20*, 53.
- (4) Wang, X.; Li, Y.; Wang, J.; Wang, Y.; Ye, J.; Yan, H.; Zhang, J.; Thomas, R. K. *J. Phys. Chem. B* **2005**, *109*, 12850.
- (5) Tarek, M.; Tobias, D. J.; Klein, M. L. *J. Phys. Chem.* **1995**, *99*, 1393.
- (6) Kuhn, H.; Rehage, H. *J. Phys. Chem. B* **1999**, *103*, 8493.
- (7) Jang, S. S.; Goddard, W. A., III. *J. Phys. Chem. B* **2006**, *110*, 7992.
- (8) Khurana, E.; Nielsen, S. O.; Klein, M. L. *J. Phys. Chem. B* **2006**, *110*, 22136.
- (9) Buuren, A. R. v.; Berendsen, H. J. C. *Langmuir* **1994**, *10*, 1703.
- (10) Dominguez, H. *J. Phys. Chem. B* **2002**, *106*, 5915.
- (11) Jang, S. S.; Lin, S.-T.; Maiti, P. K.; Blanco, M.; Goddard, W. A. G., III; Shuler, P.; Tang, Y. *J. Phys. Chem. B* **2004**, *108*, 12130.
- (12) Tarek, M.; Bandyopadhyay, S.; Klein, M. L. *J. Mol. Liq.* **1998**, *78*, 1.
- (13) Maillet, J.-B.; Lachet, V.; Coveney, P. V. *Phys. Chem. Chem. Phys.* **1999**, *1*, 5277.
- (14) Marrink, S. J.; Tieleman, D. P.; Mark, A. E. *J. Phys. Chem. B* **2000**, *104*, 12165.
- (15) Jorge, M. *Langmuir* **2008**, *24*, 5714.
- (16) Oda, R.; Laguerre, M.; Huc, I.; Desbat, B. *Langmuir* **2002**, *18*, 9659.
- (17) Klein, M. L.; Shinoda, W. *Science* **2008**, *321*, 798.
- (18) Marrink, S. J.; Vries, A. H. d.; Mark, A. E. *J. Phys. Chem. B* **2004**, *108*, 750.
- (19) Shinoda, W.; DeVane, R.; Klein, M. L. *Soft Matter* **2008**, *4*, 2454.
- (20) Smit, B.; Hilbers, P. A. J.; Esselink, K.; Rupert, L. A. M.; Os, N. M. v.; Schlijper, A. G. *Nature* **1990**, *348*, 624.
- (21) McCullagh, M.; Prytkova, T.; Tonzani, S.; Winter, N. D.; Schatz, G. C. *J. Phys. Chem. B* **2008**, *112*, 10388.
- (22) Marrink, S. J.; Risselada, H. J.; Yefimov, S.; Tieleman, D. P.; Vries, A. H. d. *J. Phys. Chem. B* **2007**, *111*, 7812.
- (23) Karaborni, S.; Esselink, K.; Hilbers, P. A. J.; Smit, B.; Karthaus, J.; Os, N. M. v.; Zana, R. *Science* **1994**, *266*, 254.
- (24) Maiti, P. K.; Chowdhury, D. *J. Chem. Phys.* **1998**, *109*, 5126.
- (25) Monticelli, L.; Kandasamy, S. K.; Periole, X.; Larson, R. G.; Tieleman, D. P.; Marrink, S.-J. *J. Chem. Theory Comput.* **2008**, *4*, 819.
- (26) Truhlar, D. G. *J. Am. Chem. Soc.* **2008**, *130*, 16824.
- (27) Hess, B.; Kutzner, C.; Spoel, D. v. d.; Lindahl, E. *J. Chem. Theory Comput.* **2008**, *4*, 435.
- (28) Bussi, G.; Donadio, D.; Parrinello, M. *J. Chem. Phys.* **2007**, *126*, 014101.
- (29) Berendsen, H. J. C.; Postma, J. P. M.; DiNola, A.; Haak, J. R. *J. Chem. Phys.* **1984**, *81*, 3684.
- (30) Jorgensen, W. L.; Chandrasekhar, J.; Madura, J. D.; Impey, R. W.; Klein, M. L. *J. Chem. Phys.* **1983**, *79*, 926.
- (31) Jorgensen, W. L.; Gao, J. *J. Phys. Chem.* **1986**, *90*, 2174.
- (32) Jorgensen, W. L.; Maxwell, D. S.; Tirado-Rives, J. *J. Am. Chem. Soc.* **1996**, *118*, 11225.
- (33) Jorgensen, W. L.; Tirado-Rives, J. *J. Am. Chem. Soc.* **1988**, *110*, 1657.
- (34) Miyamoto, S.; Kollman, P. A. *J. Comput. Chem.* **1992**, *13*, 952.
- (35) Hess, B.; Bekker, H.; Berendsen, H. J. C.; Fraaije, J. G. E. M. *J. Comput. Chem.* **1997**, *18*, 1463.
- (36) Darden, T.; York, D.; Pedersen, L. *J. Chem. Phys.* **1993**, *98*, 10089.
- (37) Essmann, U.; Perera, L.; Berkowitz, M. L.; Darden, T.; Lee, H.; Pedersen, L. G. *J. Chem. Phys.* **1995**, *103*, 8577.
- (38) Wu, R.; Deng, M.; Kong, B.; Wang, Y.; Yang, X. *J. Phys. Chem. B* **2009**, *113*, 12680.
- (39) Espert, A.; Klitzing, R. v.; Poulin, P.; Colin, A.; Zana, R.; Langevin, D. *Langmuir* **1998**, *14*, 4251.
- (40) Patist, A.; Kanicky, J. R.; Shukla, P. K.; Shah, D. O. *J. Colloid Interface Sci.* **2002**, *245*, 1.
- (41) D'Errico, G.; Ortona, O.; Paduano, L.; Vitagliano, V. *J. Colloid Interface Sci.* **2001**, *239*, 264.
- (42) Zielinski, R.; Ikeda, S.; Nomura, H.; Kato, S. *J. Colloid Interface Sci.* **1987**, *119*, 398.
- (43) Wang, X.; Wang, J.; Wang, Y.; Ye, J.; Yan, H.; Thomas, R. K. *J. Colloid Interface Sci.* **2005**, *286*, 739.
- (44) Rubinstein, M.; Colby, R. H. *Polymer Physics*, 1st ed.; Oxford University Press: USA, 2003.
- (45) Danino, D.; Talmon, Y.; Zana, R. *Langmuir* **1995**, *11*, 1448.
- (46) Maiti, P. K.; Lansac, Y.; Glaser, M. A.; Clark, N. A.; Rouault, Y. *Langmuir* **2002**, *18*, 1908.